Understanding the Impact of Wall Thickness on Thermal Stability of Silver-Gold Nanocages

Shikuan Shao,[†,#] Xiangyu Zhu,[‡,#] Victoria Ten,[§] Moon J. Kim,[‡,*] and Xiaohu Xia[†,∥,*]

[†]*Department of Chemistry, University of Central Florida, Orlando, Florida 32816, United States;*

[‡]*Department of Materials Science and Engineering, University of Texas at Dallas, Richardson, Texas 75080, United States;*

[§]*Burnett School of Biomedical Sciences, University of Central Florida, Orlando, Florida 32816, United States;*

[∥]*NanoScience Technology Center, University of Central Florida, Orlando, Florida 32816, United States.*

[#]*These two authors contributed equally to this work.*

[*]*Corresponding author. E-mails: moonkim@utdallas.edu (M.J.) and Xiaohu.Xia@ucf.edu (X.X.)*

Abstract

The thermal stability of nanocages is of great research value in both fundamental studies and practical applications. In this work, by focusing on silver-gold (Ag-Au) alloyed nanocages as a model system, we demonstrate that the wall thickness of the nanocage is a critical parameter in determining its thermal stability. We systematically evaluated the thermal stabilities of Ag-Au nanocages with different wall thicknesses in the range of 3.8-13 nm in both solution- and solid phases. The results showed that, in both phases, nanocages with thicker walls displayed better stabilities. At sufficiently high temperatures, the nanocages were deformed to thermodynamically more stable nanostructures. The deformation processes were found to be different for nanocages with various wall thicknesses, which were carefully monitored and analyzed by electron microscopy imaging. Changes in plasmonic properties of the nanocages during heat-induced deformation processes were also investigated.

TOC Graphic

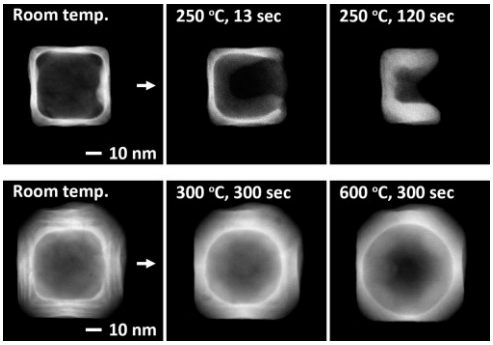

Keywords: hollow nanostructure · nanocage · wall thickness · plasmonics · stability

1. INTRODUCTION

Metallic nanocrystals with a cage structure (*i.e.*, nanocages) have been extensively studied in recent years because of their unique physicochemical properties such as large surface-to-volume ratio, highly open structure, and excellent plasmonic, photonic and/or catalytic activities.[1-4] Compared with conventional solid nanostructures, nanocages exhibited superior performances in various technologically important applications. Examples include sensing,[5-8] drug delivery,[9-11] photothermal therapies,[12-15] and energy harvesting.[16-18] In these applications, the performance of nanocages is closely associated with their morphologies and elemental compositions.[1] In many cases, nanocages experience extreme or variable temperatures during an application and thus may be subject to morphological/compositional changes.[19-22] To ensure reliable performance, nanocages should possess good thermal stability. For example, in laser-based applications,[23-25] the localized temperature of nanocages may reach several hundred degrees Celsius. Consequently, deformation and even collapse of nanocages are often observed. For plasmonic metal nanocages, they may melt upon laser excitation at the resonance frequency of their localized surface plasmon resonance (LSPR) peaks.[23] Similarly, deformation of nanocages caused by elevated temperatures may occur in photocatalysis.[26-29] In order to design and prepare functional nanocages with reliable performance, it is meaningful to understand their thermal stabilities.

In this study, using silver-gold (Ag-Au) nanocages as a model system, we demonstrate that the wall thickness plays a critical role in determining the thermal stability of nanocages. We chose to focus on Ag-Au nanocages because they have been widely studied and used in various fields such as biomedicine and catalysis.[9,13,30-35] It is worth mentioning that, to the best of our knowledge, a systematic understanding of the impact of wall thickness on Ag-Au nanocage stability from experimental aspects has not been reported so far. Previous studies on thermal stabilities of Ag-Au nanocages primarily rely on molecular dynamics (MD) simulations.[36-39] The lack of understanding from experiments can be attributed to the challenge of controlling the wall thickness of nanocage in a synthesis. In a recent study, we reported an effective strategy based on galvanic replacement and regeneration of a sacrificial template to produce Ag-Au nanocages of controllable wall thicknesses.[6] Specifically, as shown by Figure 1a, conventional singly-walled Ag-Au nanocages (obtained from the galvanic replacement reaction between Au^{3+} ions and Ag nanocubes as templates[40]) are first stuffed with Ag through selective deposition of Ag atoms on the inner surface (*i.e.*, template regeneration). Then the resultant Ag@Ag-Au core@shell nanocubes are

used as new templates for the second round of galvanic replacement with Au^{3+} ions. As a result, Ag-Au cages with a thicker wall composed of two consecutive Ag-Au layers are obtained. To differentiate the initial cages with single Ag-Au layers and subsequent cages with two consecutive Ag-Au layers, they will be referred to as "$[Ag\text{-}Au]_1$ cages" and "$[Ag\text{-}Au]_2$ cages", respectively, in the following discussion. By repeating such a process of sequential galvanic replacement and template regeneration, $[Ag\text{-}Au]_n$ cages (n: number of consecutive Ag-Au layers) with increasing wall thicknesses can be prepared as a function of n.

To study the effect of wall thickness on the thermal stability of Ag-Au nanocages, in this work, we synthesized $[Ag\text{-}Au]_n$ cages (n = 1-4) that have wall thicknesses in the range of 3.8-13 nm. The experiments of the thermal stability study were conducted in both solution and solid phases. The solution-phase tests were performed in diethylene glycol with a relatively high boiling point (~244 ^oC[41]). The solid-phase tests were achieved by *in-situ* heating scanning transmission electron microscopy (STEM). In addition to morphological changes of cages under different temperatures, we also investigated the changes of plasmonic properties and elemental compositions.

2. METHODS

2.1. Chemicals and Materials. Silver nitrate ($AgNO_3$, ⩾99.0%), gold (III) chloride trihydrate ($HAuCl_4 \cdot 3H_2O$, ⩾99.9%), poly(vinylpyrrolidone) (PVP55, Mw ≈ 55,000), sodium hydrosulfide hydrate ($NaHS \cdot xH_2O$), L-ascorbic acid (AA, ⩾99%), diethylene glycol (⩾99.0%) and sodium chloride (NaCl, ⩾99.5%) were all obtained from Sigma-Aldrich. Ethylene glycol (EG) was obtained from J. T. Baker. Deionized (DI) water with a resistivity of 18.2 MΩ·cm was used to prepare all the aqueous solutions. All materials were used without any further purification.

2.2. Synthesis of Ag Nanocubes. Ag cubes with an average edge length of 47.6 nm were synthesized according to previously reported methods with minor modifications[40,42]. Briefly, 9.0 mL of ethylene glycol (EG) was first added to a 50-mL glass vial and preheated to 150 °C in an oil bath under magnetic stirring for 1 h. Subsequently, 120 μL of 3 mM NaHS solution (in EG) was injected into the glass vial using a pipet. After 8 min, 2.25 mL of PVP55 solution (20 mg/mL, in EG) was injected, followed by the addition of 0.75 mL of $AgNO_3$ (282 mM, in EG) solution. The products (*i.e.*, 47.6 nm Ag cubes) were obtained by quenching the reaction with an ice-water bath when the reaction suspension turned into a brown color with a major localized surface

plasmon resonance (LSPR) peak at ~446 nm. The suspension was then washed with acetone once and DI water twice via centrifugation. Finally, the 47.6 nm Ag cubes were dispersed in 4.0 mL of DI water for future use.

2.3. Synthesis of [Ag-Au]$_1$ Cages. The [Ag-Au]$_1$ cages were synthesized based on the galvanic replacement reaction between above mentioned 47.6 nm Ag cubes as sacrificial templates and $HAuCl_4$, according to a published protocol with modifications.[40] In a typical synthesis, 1.0 mL of 47.6 nm Ag cubes and 10 mL of 0.5% (w/v) PVP55 aqueous solution were first mixed in a 25-mL round-bottom flask and preheated to 95 ^oC in an oil bath under magnetic stirring for 15 min. Then, 6.0 mL of 0.02% (w/v) $HAuCl_4$ solution was injected into the flask at a rate of 100 μL/min using a syringe pump. After complete injection of $HAuCl_4$ solution, the reaction mixture was kept stirring at 95 ^oC for 10 minutes. The [Ag-Au]$_1$ cages as final product were collected by centrifugation, washed once with saturated NaCl solution, and 10 times with DI water. Finally, the [Ag-Au]$_1$ cages were dispersed in 1.0 mL of DI water and stored in the dark for future use.

2.4. Synthesis of [Ag-Au]$_n$ Cages (n = 2, 3, and 4). The [Ag-Au]$_n$ cages (n = 2, 3, and 4) were prepared through the strategy of sequential processes of template regeneration and galvanic replacement, according to our recently reported protocol with minor modifications.[6] Specifically, to prepare [Ag-Au]$_2$ cages, 1.0 mL of above mentioned [Ag-Au]$_1$ cage was mixed with 5 mL of DI water in a 20 mL-glass vial at room temperature under magnetic stirring. Subsequently, 5 mM $AgNO_3$ and 2.5 mM AA aqueous solution were injected simultaneously at a 5 μL/min rate using a two-channel syringe pump. The reaction was terminated when the major LSPR peak of the solution stopped shifting to shorter wavelengths. The Ag@Ag-Au core@shell nanocubes as products were collected via centrifugation and redispersed in 1.0 mL DI water. The as-synthesized Ag@Ag-Au nanocubes were then used as sacrificial templates to synthesize [Ag-Au]$_2$ cages by following the same galvanic replacement procedure used to synthesize [Ag-Au]$_1$ cages.

[Ag-Au]$_3$ cages and [Ag-Au]$_4$ cages, respectively, were obtained by conducting one and two more rounds of template regeneration plus the galvanic replacement based on the synthesis of [Ag-Au]$_2$ cages. Detailed synthetic procedures can be found in our previous publications.[5,6]

2.5. Solution-Phase Heating Experiment. For solution-phase thermal stability tests, 250 μL of [Ag-Au]$_n$ cage (n = 1-4) samples were centrifuged and redispersed in 3.0 mL of diethylene glycol. The solutions were then immersed in an oil bath under magnetic stirring at different temperatures

(150 ºC, 175 ºC, and 200 ºC). Aliquots were taken at different incubation times (*e.g.*, 5 min, 15 min, 30 min, 45 min, and 60 min) using glass pipets and were quickly transferred to glass vials placed in an ice bath. Each thoroughly cooled aliquot was divided into two parts: one part was transferred to a cuvette, diluted with DI water, and subjected to measurement of LSPR peaks with a UV-Vis spectrophotometer (Agilent Cary 60 UV-vis spectrophotometer); the other part was washed with acetone once and DI water twice via centrifugation. This sample was collected for morphological analyses with a transmission electron microscope (JEOL JEM-1011 microscope operated at 100 kV).

2.6. *In-situ* Scanning Transmission Electron Microscopy (STEM) Heating Experiment. *In-situ* STEM heating experiments were performed on an Aduro specimen holder with heating E-chips supplied by Protochips Inc., which allowed for heating samples from room temperature (RT) up to 1200 ºC with low drift. The accuracy of the applied temperature on the Protochips heating E-chips was less than 5 °C. The nanocage sample was drop cast on a carbon thin film window on the heating E-chips for observation, where the temperature was increased with 50 ºC gradient and 5-minute holding time until the nanocage collapsed. The base chamber pressure of the microscope was ~1.5×10^{-6} mbar. STEM imaging was performed using a JEM-ARM200F (JEOL USA Inc.) equipped with a spherical aberration (Cs) corrector (CEOS GmbH, Heidelberg, Germany). The microscope was operated at 200 kV, and the probe convergence semi-angle was 23 mrad with a probe current of 18 pA. The acquisition semi-angle for high-angle annular dark-field (HAADF) detector was 70-200 mrad. The corrector had been carefully tuned by the Zemlin-tableau method with Cs = 0.5 μm, at which the resolution was about 1 Å. Energy Dispersive X-ray Spectroscopy (EDS) was performed with an Oxford X-MaxN100TLE with 100 mm^2 silicon drift detector. To avoid the oversaturation of the EDS detector, the spectrum data was collected after quenching the sample to RT.

3. RESULTS AND DISCUSSION

3.1. Synthesis and Characterizations of $[Ag\text{-}Au]_n$ Cages of Different Wall Thicknesses. The $[Ag\text{-}Au]_1$ cages were synthesized from a galvanic replacement reaction between 47.6 nm Ag cubes (see Figure S1) and $HAuCl_4$.[40] The $[Ag\text{-}Au]_n$ cages (n = 2, 3, and 4) were synthesized through the processes of sequential galvanic replacement and template regeneration.[6] Figure 1b-e

shows typical TEM images of as-synthesized [Ag-Au]$_n$ cages (n = 1-4). It can be seen that the cages had similar void shapes/sizes but different wall thicknesses. By randomly analyzing 200 particles for each sample, the average sizes (L, defined as the distance between two opposite {100} facets of a cage[6]) of the four [Ag-Au]$_n$ cages (n = 1, 2, 3, and 4) were measured to be 52.3, 58.6, 65.6, and 72.7 nm, respectively. Their average wall thicknesses (t) were measured to be 3.8, 7.2, 10.2, and 13.0 nm, respectively. These measurements indicate that the void sizes of all [Ag-Au]$_n$ cages were similar. The EDS analysis data shown in Figure S2 suggest that all the [Ag-Au]$_n$ cages (n = 1-4) had similar molar ratios of Ag to Au (roughly 1:1). As indicated by the EDS analyses of individual cages (which will be discussed later) and our previous published work,[6] Ag and Au co-exist in the cages in the form of alloy. Collectively, these four types of Ag-Au cages, which have similar void sizes and elemental compositions, but different wall thicknesses, could serve as an ideal platform to investigate the impact of wall thickness on the thermal stability of nanocages.

3.2. Solution-Phase Stability Tests. To evaluate the thermal stabilities of cages in the solution phase, the four [Ag-Au]$_n$ cages (n = 1, 2, 3, and 4) were dispersed in diethylene glycol and heated at 150 ºC, 175 ºC, and 200 ºC for certain periods of time. Morphological changes of the cages were checked by transmission electron microscopy (TEM) imaging. Figure 2a-t shows representative TEM images of the [Ag-Au]$_n$ cages after they had been heated at 175 ºC for 5, 15, 30, 45, and 60 minutes. The overall trend is that the thicker the walls are, the better the cages can preserve their original morphologies (*e.g.*, cubic shape and hollow interior). Specially, [Ag-Au]$_1$ cages started to deform at 5 min and completely collapsed and lost their cage-like morphology at 60 min. In contrast, the [Ag-Au]$_4$ cages well preserved the overall cage morphology during the entire process, despite slight truncations at corners and edges. The [Ag-Au]$_2$ and [Ag-Au]$_3$ cages started to deform at 15 and 30 min, respectively. Similar trends were observed during the treatments of cages at 150 ºC (Figure S3) and 200 ºC (Figure S4).

Taking the treatment of [Ag-Au]$_1$ cages at 175 ºC as an example, a typical deformation process of cages during heat treatment includes the following stages: the small pores in the side faces and corners of original cages tended to enlarge in size (Figure 2a). These pores then merged together in the side faces to form larger pores (Figure 2b). Meanwhile, Ag and Au atoms on side faces of cages migrated to edges and corners. Later on, the cages were transformed into cubic frames (Figure 2c). Under continuous thermal stress, the frames fractured at some edges and shrank into

U-shaped nanostructures (Figure 2d). During this process, the frames were thickened, indicating the inner-particle migration of Ag and Au atoms. Continued migration of atoms eventually transformed the U-shaped nanostructures into pseudospherical nanostructures (Figure 2e). A scheme that summarizes the deformation processes is provided in Figure S5. It should be noted that, under more intense thermal stress (*e.g.*, 200 °C), the pseudospherical nanostructures were transformed into nearly spherical nanoparticles (see Figure S4).

We believe the abovementioned deformation of cages is a thermodynamically driven process. The mechanism can be understood from an energetic consideration. The total free energy (ΔG_{total}) driving the deformation of cages is primarily contributed by two factors – the volumetric free energy (ϵ_{volume}) and the surface free energy ($\epsilon_{surface}$).[43,44] In this study, the volumetric free energy remains the same during the process of cage deformation because the bulk volume of atoms in a particle is unchanged.[19] Therefore, total free energy is dependent on the surface free energy ($\epsilon_{surface}$). For Ag-Au cages that take a face-centered-cubic crystal structure,[45,46] $\epsilon_{surface}$ can be expressed by the following equation:[43]

$$\epsilon_{surface} = \sum_{n} A_n \gamma_n = A_{\{100\}}\gamma_{\{100\}} + A_{\{110\}}\gamma_{\{110\}} + A_{\{111\}}\gamma_{\{111\}} + \cdots$$

Wherein, A_n and γ_n refer to the total surface area and the surface free energy per unit area of a given crystallographic facet, respectively. Nanocages possess a much larger surface area (including both outer and inner surfaces) than their solid counterparts of the same dimensions. Under thermal treatment, nanoparticles with a lower total free energy (ΔG_{total}) are thermodynamically favored. Therefore, the cages tend to undergo structural changes that can minimize A_n in order to reduce $\epsilon_{surface}$ and thus ΔG_{total}, which can be interpreted as the attempt to reduce the surface-to-volume ratio. Cages are transformed into frames through the migration of atoms from side faces to edges and corners. With sufficiently high thermal energy, the frames could further transform into spheres with a minimal surface-to-volume ratio.

3.3. LSPR Properties. Ag-Au cages possess intriguing and useful LSPR properties.[5,13,35] It is well-known that the plasmonic properties of Ag-Au cages have a strong dependence on their morphology. Therefore, we also monitored the plasmonic activities of cages during heat treatment. Experimentally, samples were collected at different stages of solution-phase heat treatment, diluted

with DI water, and subjected to measurements with a UV-Vis spectrophotometer. Figure 3a-l compares normalized UV-vis spectra of the four [Ag-Au]$_n$ cages (n = 1, 2, 3, and 4) before and after they had been heated at different temperatures for certain periods of time. A general trend observed in the spectra change is that major LSPR peaks shift to shorter wavelengths (blue shift) as temperature and/or incubation time increase. More specifically, at 150 ºC (Figure 3a), the major LSPR peak of [Ag-Au]$_1$ cages gradually shifted from ~730 nm to ~650 nm during 5-60 min. Meanwhile, the peak was broadened as the heating time increased. Slight blue shifts of LSPR peaks were observed for [Ag-Au]$_2$ and [Ag-Au]$_3$ cages (Figure 3d,g). In contrast, the peak of [Ag-Au]$_4$ LSPR remained unchanged (Figure 3j). In general, the major LSPR peaks of a nanocage tend to blue shift when its degree of hollowness is decreased.[1,2,6,47] In this regard, these observations of LSPR peak changes are consistent with the TEM imaging results (Figure S3). At 175 ºC (Figure 3b), the major LSPR peaks of [Ag-Au]$_1$ cages were kept at ~730 nm during 0-30 min, while the bandwidth was gradually broadened. At 45 min and 60 min, the major peaks blue-shifted to ~600 nm and ~480 nm, respectively. Slight blue shifts along with peak broadening were observed for the [Ag-Au]$_2$ and [Ag-Au]$_3$ cages during 5-60 min (Figure 3e,h). As for the [Ag-Au]$_4$ cages, appreciable changes of LSPR peaks could only be observed at 45 and 60 min (Figure 3k). At 200 ºC, blue shift and peak broadening for the LSPR peaks of [Ag-Au]$_1$, [Ag-Au]$_2$ and [Ag-Au]$_3$ cages became more evident (Figure 3c,f,i). The LSPR peaks of [Ag-Au]$_4$ cages were gradually broadened while not blue-shifted significantly (Figure 3l). Overall, these results demonstrated that Ag-Au cages with thicker walls tend to better preserve their LSPR activities at high temperatures.

3.4. *In-situ* Heating STEM Tests. *In-situ* STEM heating experiments were performed to reveal detailed morphological and compositional changes for single cages at atomic precision. [Ag-Au]$_1$ and [Ag-Au]$_4$ cages as two representative examples with distinctively different wall thicknesses were analyzed and compared.

Figure 4a-d shows STEM analyses data of an individual [Ag-Au]$_1$ cage after heated at 200 and 250 ºC for up to 5 minutes. Before heating (Figure 4a), the [Ag-Au]$_1$ cage displayed a well-defined cubic shape (a square projection image) with an edge length of ~50 nm and a wall thickness of ~4 nm. The EDS mapping images show that the cage is made of Ag-Au alloy with overall homogeneous distributions of Ag and Au across the entire particle. The cage preserved its morphology and elemental compositions after being heated at 200 ºC for 5 min (see Figure 4b). It

should be noted that, at the same temperature and heating time, the $[Ag\text{-}Au]_1$ cages deformed to frames when they were suspended in solution. This difference might be ascribed to the fact that the *in-situ* STEM heating experiment was performed in a more inert environment (*e.g.*, without oxygen and solvent). Thus the cage was expected to withstand heating at a higher temperature. When the temperature was elevated to 250 ºC (Figure 4c), the cage was deformed to a U-shaped nanostructure at 5 min. The EDS mapping images show that such a nanostructure was composed of Ag-Au alloy, implying that Ag and Au were not segregated during deformation. Time-resolved deformation dynamics were recorded with serial images (Figure 4d). It was revealed that the cage started to collapse from one side face immediately after heating and propagated to the whole particle within 50 seconds. During this process, atoms of collapsing side face migrated to other sites of the cage, leading to the formation of a U-shaped nanostructure. The continuous migration of atoms (120-210 seconds) thickened the frames of such a U-shaped nanostructure.

Compared to $[Ag\text{-}Au]_1$ cage, the $[Ag\text{-}Au]_4$ cage was much more stable during the *in-situ* STEM heating test (see Figure 5a-h). Before heating (Figure 5a), the edge length and wall thickness of $[Ag\text{-}Au]_4$ cage were measured to be ~70 nm and ~10 nm, respectively. EDS mapping images (Figure S6a) suggest the cage is made of Ag-Au alloys. Notably, the four consecutive Ag-Au layers in this cage can be seen from the STEM image, where each layer was composed of an Au-rich (with a brighter contrast) and an Ag-rich sub-layers. The alternating Au and Ag sublayers could be clearly seen from the magnified STEM image (Figure 5e) and the EDS line-scan profile (Figure 5f). This inhomogeneous distribution of Au and Ag could be ascribed to the sequential galvanic replacement and template regeneration processes during cage synthesis.[1,6] The $[Ag\text{-}Au]_4$ cage could maintain the cubic shape and wall thickness very well after annealing for 5 minutes at 300 ºC (Figure 5b). Notably, the distribution of Ag and Au in the wall became homogeneous, which was evidenced by the STEM imaging contrast (Figure 5g) and EDS line-scan profile (Figure 5h). A careful examination indicated that some atoms on the walls had migrated to the corner sites of the cubic hollow interior along the <111> directions, leading to a round projection of the interior. These observations suggest that Ag and Au atoms inter-diffused in the wall and, in the meantime, the atoms migrated to the interior. The cage could still preserve its overall cubic shape after it had been heated at 600 ºC for 5 min (Figure 5c). Notably, compared to the cage after 300 ºC annealing for 5 minutes (sample in Figure 5b), thicknesses of the walls along the side faces were decreased while the exterior size of the cage remained unchanged. These observations imply that the atoms

in the inner walls had migrated to the corner sites of the cubic hollow interior. Shortly after the temperature was elevated to 650 ºC (for 1 min), the cage was transformed into a solid particle with a polyhedral shape. Detailed processes of such a transformation from the cage to a solid polyhedron and associated mechanism were not studied in the present work, which may be the subjects of our future research. Ag and Au existed in the form of alloy throughout the whole heating process, as shown by the EDS mapping images in Figure S6.

Overall, the $[Ag\text{-}Au]_4$ cage with thicker walls exhibited enhanced thermal stability in the *in-situ* heating STEM tests compared with the $[Ag\text{-}Au]_1$ cage. Despite the difference in deformation processes of both cages, they eventually evolved into nanostructures with reduced total surface areas and thus lower total free energies.

4. CONCLUSIONS

In summary, we have systematically investigated the impact of wall thickness on the thermal stability of Ag-Au nanocages. $[Ag\text{-}Au]_n$ cages (n: number of consecutive Ag-Au layers) with well-defined cubic shapes and different wall thicknesses (which increases as n increases) were used as models. The thermal stability tests were performed in both solution- and solid phases. We found that, in both phases, cages with thicker walls exhibited better thermal stabilities than those with thinner walls. In a sense, the thermal stability of Ag-Au cages could be effectively enhanced by thickening their walls. This finding may help researchers design more stable and reliable nanocages for specific applications. The heat-induced deformation processes of cages with different wall thicknesses were found to be different. Nevertheless, all cages were eventually transformed into thermodynamically more stable nanostructures. The changes in plasmonic properties of cages during thermal treatment were also examined. The insights from this study may serve as a solid foundation to inspire future fundamental and applied research.

Supporting Information

The Supporting Information is available free of charge on the ACS Publications website.

- TEM image of Ag nanocubes; EDS spectra taken from nanocages; TEM images of nanocages after they had been heated in solution at 150 ºC and 200 ºC for different periods of time; HAADF-STEM images and EDS mapping images recorded from the same cage after it had been heated at different temperatures in STEM for certain periods of time.

Acknowledgments

This work was supported in part by a grant from the National Science Foundation (DMR-2004546) and startup funds from the University of Central Florida (UCF).

Competing Interests

The authors declare no competing interests.

References

1. Xia, X.; Wang, Y.; Ruditskiy, A.; Xia, Y. 25th Anniversary Article: Galvanic Replacement: A Simple and Versatile Route to Hollow Nanostructures with Tunable and Well-Controlled Properties. *Adv. Mater.* **2013**, *25*, 6313-6333.
2. Genç, A.; Patarroyo, J.; Sancho-Parramon, J.; Bastús, N. G.; Puntes, V.; Arbiol, J. Hollow Metal Nanostructures for Enhanced Plasmonics: Synthesis, Local Plasmonic Properties and Applications. *Nanophotonics* **2017**, *6*, 193-213.
3. Tong, L.; Cobley, C. M.; Chen, J.; Xia, Y.; Cheng, J. Bright Three-Photon Luminescence from Gold/Silver Alloyed Nanostructures for Bioimaging with Negligible Photothermal Toxicity. *Angew. Chem. Int. Ed.* **2010**, *49*, 3485-3488.
4. Cobley, C. M.; Xia, Y. Engineering the Properties of Metal Nanostructures via Galvanic Replacement Reactions. *Mater. Sci. Eng. R Rep.* **2010**, *70*, 44-62.
5. Gao, Z.; Shao, S.; Gao, W.; Tang, D.; Tang, D.; Zou, S.; Kim, M. J.; Xia, X. Morphology-Invariant Metallic Nanoparticles with Tunable Plasmonic Properties. *ACS Nano* **2021**, *15*, 2428-2438.
6. Gao, Z.; Ye, H.; Wang, Q.; Kim, M. J.; Tang, D.; Xi, Z.; Wei, Z.; Shao, S.; Xia, X. Template Regeneration in Galvanic Replacement: A Route to Highly Diverse Hollow Nanostructures. *ACS Nano* **2020**, *14*, 791-801.
7. Koo, W.-T.; Cha, J.-H.; Jung, J.-W.; Choi, S.-J.; Jang, J.-S.; Kim, D.-H.; Kim, I.-D. Few-Layered WS_2 Nanoplates Confined in Co, N-Doped Hollow Carbon Nanocages: Abundant WS_2 Edges for Highly Sensitive Gas Sensors. *Adv. Funct. Mater.* **2018**, *28*, 1802575.
8. Zeng, Y.; Zhang, T.; Fan, H.; Fu, W.; Lu, G.; Sui, Y.; Yang, H. One-Pot Synthesis and Gas-

Sensing Properties of Hierarchical $ZnSnO_3$ Nanocages. *J. Phys. Chem. C* **2009**, *113*, 19000-19004.

9. Yavuz, M. S.; Cheng, Y.; Chen, J.; Cobley, C. M.; Zhang, Q.; Rycenga, M.; Xie, J.; Kim, C.; Song, K. H.; Schwartz, A. G. *et al.* Gold Nanocages Covered by Smart Polymers for Controlled Release with Near-Infrared Light. *Nat. Mater.* **2009**, *8*, 935-939.
10. Hu, F.; Zhang, Y.; Chen, G.; Li, C.; Wang, Q. Double-Walled Au Nanocage/SiO_2 Nanorattles: Integrating SERS Imaging, Drug Delivery and Photothermal Therapy. *Small* **2015**, *11*, 985-993.
11. Wang, C.; Wang, Y.; Zhang, L.; Miron, R. J.; Liang, J.; Shi, M.; Mo, W.; Zheng, S.; Zhao, Y.; Zhang, Y. Pretreated Macrophage-Membrane-Coated Gold Nanocages for Precise Drug Delivery for Treatment of Bacterial Infections. *Adv. Mater.* **2018**, *30*, 1804023.
12. Kennedy, L. C.; Bickford, L. R.; Lewinski, N. A.; Coughlin, A. J.; Hu, Y.; Day, E. S.; West, J. L.; Drezek, R. A. A New Era for Cancer Treatment: Gold-Nanoparticle-Mediated Thermal Therapies. *Small* **2011**, *7*, 169-183.
13. Xia, Y.; Li, W.; Cobley, C. M.; Chen, J.; Xia, X.; Zhang, Q.; Yang, M.; Cho, E. C.; Brown, P. K. Gold Nanocages: From Synthesis to Theranostic Applications. *Acc. Chem. Res.* **2011**, *44*, 914-924.
14. Abadeer, N. S.; Murphy, C. J. Recent Progress in Cancer Thermal Therapy Using Gold Nanoparticles. *J. Phys. Chem. C* **2016**, *120*, 4691-4716.
15. Chen, J.; Glaus, C.; Laforest, R.; Zhang, Q.; Yang, M.; Gidding, M.; Welch, M. J.; Xia, Y. Gold Nanocages as Photothermal Transducers for Cancer Treatment. *Small* **2010**, *6*, 811-817.
16. Wang, J.; Cui, Y.; Wang, D. Design of Hollow Nanostructures for Energy Storage, Conversion and Production. *Adv. Mater.* **2019**, *31*, 1801993.
17. da Silva, A. G. M.; Rodrigues, T. S.; Haigh, S. J.; Camargo, P. H. C. Galvanic Replacement Reaction: Recent Developments for Engineering Metal Nanostructures towards Catalytic Applications. *Chem. Commun.* **2017**, *53*, 7135-7148.
18. Zhang, H.; Jin, M.; Liu, H.; Wang, J.; Kim, M. J.; Yang, D.; Xie, Z.; Liu, J.; Xia, Y. Facile Synthesis of Pd–Pt Alloy Nanocages and Their Enhanced Performance for Preferential Oxidation of CO in Excess Hydrogen. *ACS Nano* **2011**, *5*, 8212-8222.
19. Li, J.-M.; Yang, Y.; Qin, D. Hollow Nanocubes Made of Ag–Au alloys for SERS Detection with Sensitivity of 10^{-8} M for Melamine. *J. Mater. Chem. C* **2014**, *2*, 9934-9940.

20. Albrecht, W.; Bladt, E.; Vanrompay, H.; Smith, J. D.; Skrabalak, S. E.; Bals, S. Thermal Stability of Gold/Palladium Octopods Studied in Situ in 3D: Understanding Design Rules for Thermally Stable Metal Nanoparticles. *ACS Nano* **2019**, *13*, 6522-6530.
21. Vara, M.; Wang, X.; Howe, J.; Chi, M.; Xia, Y. Understanding the Stability of Pt-Based Nanocages under Thermal Stress Using In Situ Electron Microscopy. *ChemNanoMat* **2018**, *4*, 112-117.
22. Lyu, Z.; Chen, R.; Mavrikakis, M.; Xia, Y. Physical Transformations of Noble-Metal Nanocrystals upon Thermal Activation. *Acc. Chem. Res.* **2021**, *54*, 1-10.
23. Hood, Z. D.; Kubelick, K. P.; Gilroy, K. D.; Vanderlaan, D.; Yang, X.; Yang, M.; Chi, M.; Emelianov, S. Y.; Xia, Y. Photothermal Transformation of Au-Ag Nanocages under Pulsed Laser Irradiation. *Nanoscale* **2019**, *11*, 3013-3020.
24. Link, S.; Burda, C.; Nikoobakht, B.; El-Sayed, M. A. Laser-Induced Shape Changes of Colloidal Gold Nanorods Using Femtosecond and Nanosecond Laser Pulses. *J. Phys. Chem. B* **2000**, *104*, 6152-6163.
25. Huang, X.; El-Sayed, I. H.; Qian, W.; El-Sayed, M. A. Cancer Cell Imaging and Photothermal Therapy in the Near-Infrared Region by Using Gold Nanorods. *J. Am. Chem. Soc.* **2006**, *128*, 2115-2120.
26. Teranishi, M.; Naya, S.-i.; Tada, H. Temperature- and pH-Dependence of Hydrogen Peroxide Formation from Molecular Oxygen by Gold Nanoparticle-Loaded Titanium(IV) Oxide Photocatalyst. *J. Phys. Chem. C* **2016**, *120*, 1083-1088.
27. Mukherjee, S.; Zhou, L.; Goodman, A. M.; Large, N.; Ayala-Orozco, C.; Zhang, Y.; Nordlander, P.; Halas, N. J. Hot-Electron-Induced Dissociation of H_2 on Gold Nanoparticles Supported on SiO_2. *J. Am. Chem. Soc.* **2014**, *136*, 64-67.
28. Bora, T.; Zoepfl, D.; Dutta, J. Importance of Plasmonic Heating on Visible Light Driven Photocatalysis of Gold Nanoparticle Decorated Zinc Oxide Nanorods. *Sci. Rep.* **2016**, *6*, 26913.
29. Sarina, S.; Waclawik, E. R.; Zhu, H. Photocatalysis on Supported Gold and Silver Nanoparticles under Ultraviolet and Visible Light Irradiation. *Green Chem.* **2013**, *15*, 1814-1833.
30. Skrabalak, S. E.; Chen, J.; Au, L.; Lu, X.; Li, X.; Xia, Y. Gold Nanocages for Biomedical Applications. *Adv. Mater.* **2007**, *19*, 3177-3184.

31. Xia, X.; Xia, Y. Gold Nanocages as Multifunctional Materials for Nanomedicine. *Front. Phys.* **2014**, *9*, 378-384.
32. Qin, Z.; Zheng, Y.; Du, T.; Wang, Y.; Gao, H.; Quan, J.; Zhang, Y.; Du, Y.; Yin, L.; Wang, X. *et al.* Cysteamine: A Key to Trigger Aggregation-Induced NIR-II Photothermal Effect and Silver Release Booming of Gold-Silver Nanocages for Synergetic Treatment of Multidrug-Resistant Bacteria Infection. *Chem. Eng. J.* **2021**, *414*, 128779.
33. Zhang, L.; Pan, J.; Long, Y.; Li, J.; Li, W.; Song, S.; Shi, Z.; Zhang, H. CeO_2-Encapsulated Hollow Ag-Au Nanocage Hybrid Nanostructures as High-Performance Catalysts for Cascade Reactions. *Small* **2019**, *15*, 1903182.
34. Nazemi, M.; El-Sayed, M. A. The Role of Oxidation of Silver in Bimetallic Gold–Silver Nanocages on Electrocatalytic Activity of Nitrogen Reduction Reaction. *J. Phys. Chem. C* **2019**, *123*, 11422-11427.
35. Skrabalak, S. E.; Chen, J.; Sun, Y.; Lu, X.; Au, L.; Cobley, C. M.; Xia, Y. Gold Nanocages: Synthesis, Properties, and Applications. *Acc. Chem. Res.* **2008**, *41*, 1587-1595.
36. Valencia, F. J.; Ramirez, M.; Varas, A.; Rogan, J.; Kiwi, M. Thermal Stability of Hollow Porous Gold Nanoparticles: A Molecular Dynamics Study. *J. Chem. Inf. Model.* **2020**, *60*, 6204-6210.
37. Jiang, L.; Yin, X.; Zhao, J.; Liu, H.; Liu, Y.; Wang, F.; Zhu, J.; Boey, F.; Zhang, H. Theoretical Investigation on the Thermal Stability of Hollow Gold Nanoparticles. *J. Phys. Chem. C* **2009**, *113*, 20193-20197.
38. Valencia, F. J.; Ramírez, M.; Varas, A.; Rogan, J. Understanding the Stability of Hollow Nanoparticles with Polycrystalline Shells. *J. Phys. Chem. C* **2020**, *124*, 10143-10149.
39. Castro-Palacio, J. C.; Ladutenko, K.; Prada, A.; Gonzalez-Rubio, G.; Diaz-Nunez, P.; Guerrero-Martinez, A.; Fernandez de Cordoba, P.; Kohanoff, J.; Perlado, J. M.; Pena-Rodriguez, O.; Rivera, A. Hollow Gold Nanoparticles Produced by Femtosecond Laser Irradiation. *J. Phys. Chem. Lett.* **2020**, *11*, 5108-5114.
40. Skrabalak, S. E.; Au, L.; Li, X.; Xia, Y. Facile Synthesis of Ag Nanocubes and Au Nanocages. *Nat. Protoc.* **2007**, *2*, 2182-2190.
41. Winek, C. L.; Shingleton, D. P.; Shanor, S. P. Ethylene and Diethylene Glycol Toxicity. *Clin. Toxicol.* **1978**, *13*, 297-324.
42. Siekkinen, A. R.; McLellan, J. M.; Chen, J.; Xia, Y. Rapid Synthesis of Small Silver

Nanocubes by Mediating Polyol Reduction with A Trace Amount of Sodium Sulfide or Sodium Hydrosulfide. *Chem. Phys. Lett.* **2006**, *432*, 491-496.

43. Patala, S.; Marks, L. D.; Olvera de la Cruz, M. Thermodynamic Analysis of Multiply Twinned Particles: Surface Stress Effects. *J. Phys. Chem. Lett.* **2013**, *4*, 3089-3094.
44. Thanh, N. T.; Maclean, N.; Mahiddine, S. Mechanisms of Nucleation and Growth of Nanoparticles in Solution. *Chem. Rev.* **2014**, *114*, 7610-7630.
45. Tran, R.; Xu, Z.; Radhakrishnan, B.; Winston, D.; Sun, W.; Persson, K. A.; Ong, S. P. Surface Energies of Elemental Crystals. *Sci. Data* **2016**, *3*, 160080.
46. Boukouvala, C.; Ringe, E. Wulff-Based Approach to Modeling the Plasmonic Response of Single Crystal, Twinned, and Core-Shell Nanoparticles. *J. Phys. Chem. C* **2019**, *123*, 25501-25508.
47. Russo, L.; Merkoçi, F.; Patarroyo, J.; Piella, J.; Merkoçi, A.; Bastús, N. G.; Puntes, V. Time- and Size-Resolved Plasmonic Evolution with nm Resolution of Galvanic Replacement Reaction in AuAg Nanoshells Synthesis. *Chem. Mater.* **2018**, *30*, 5098-5107.

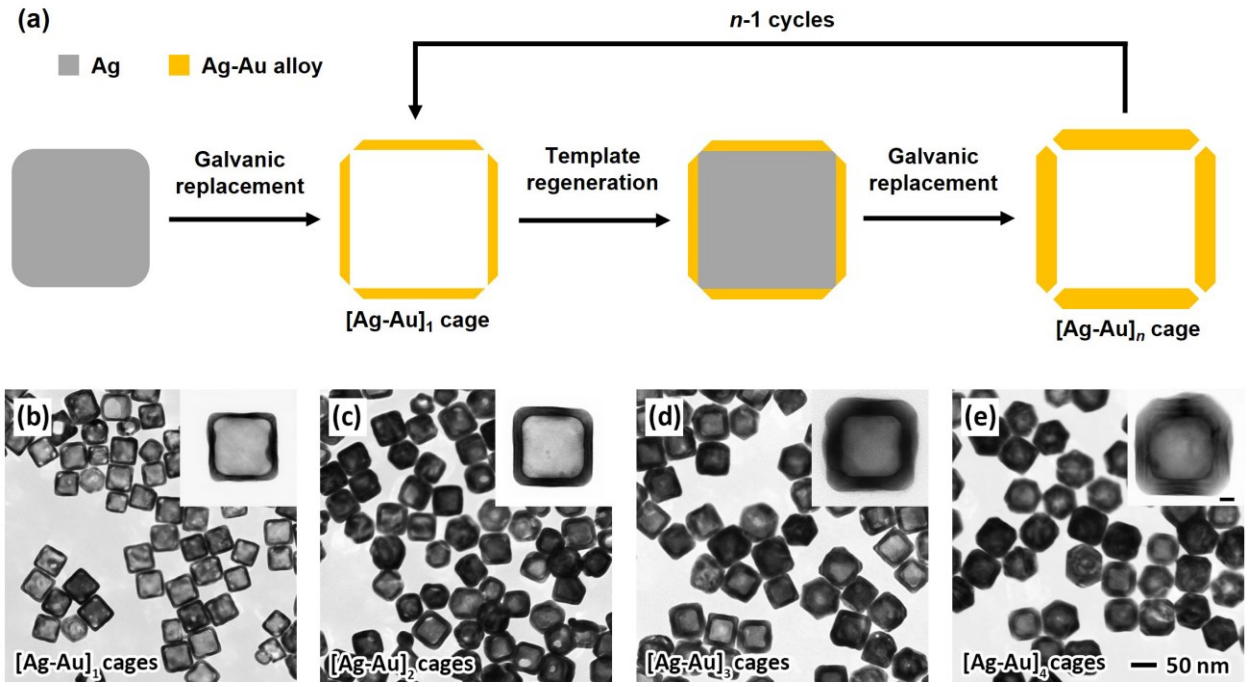

Figure 1. Synthesis and characterization of [Ag-Au]$_n$ cages (n: number of consecutive Ag-Au layers) with different wall thicknesses. (a) Schematics showing the synthetic route of [Ag-Au]$_n$ cages; (b-e) TEM images of [Ag-Au]$_n$ cages (n = 1, 2, 3, and 4). Insets show individual cages at a higher magnification. The scale bar in inset of (e) is 10 nm. The scale bars in (e) apply to all images in (b-d).

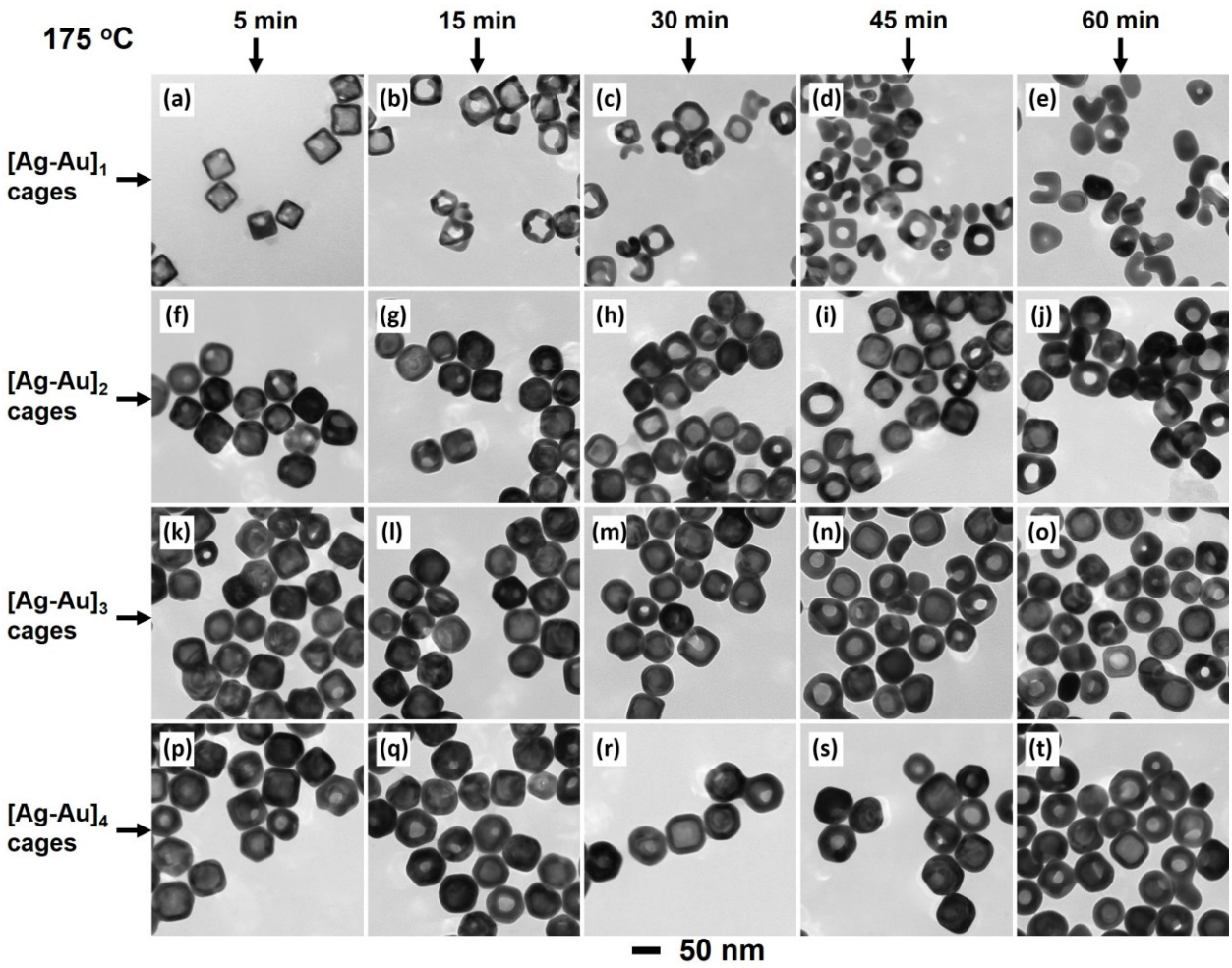

Figure 2. TEM images of $[Ag\text{-}Au]_n$ cages (n = 1, 2, 3, and 4) after they had been heated at 175 °C in diethylene glycol for different periods of time. (a-e) $[Ag\text{-}Au]_1$ cages; (f-j) $[Ag\text{-}Au]_2$ cages; (k-o) $[Ag\text{-}Au]_3$ cages; (p-t) $[Ag\text{-}Au]_4$ cages. The 50 nm scale bar applies to all TEM images.

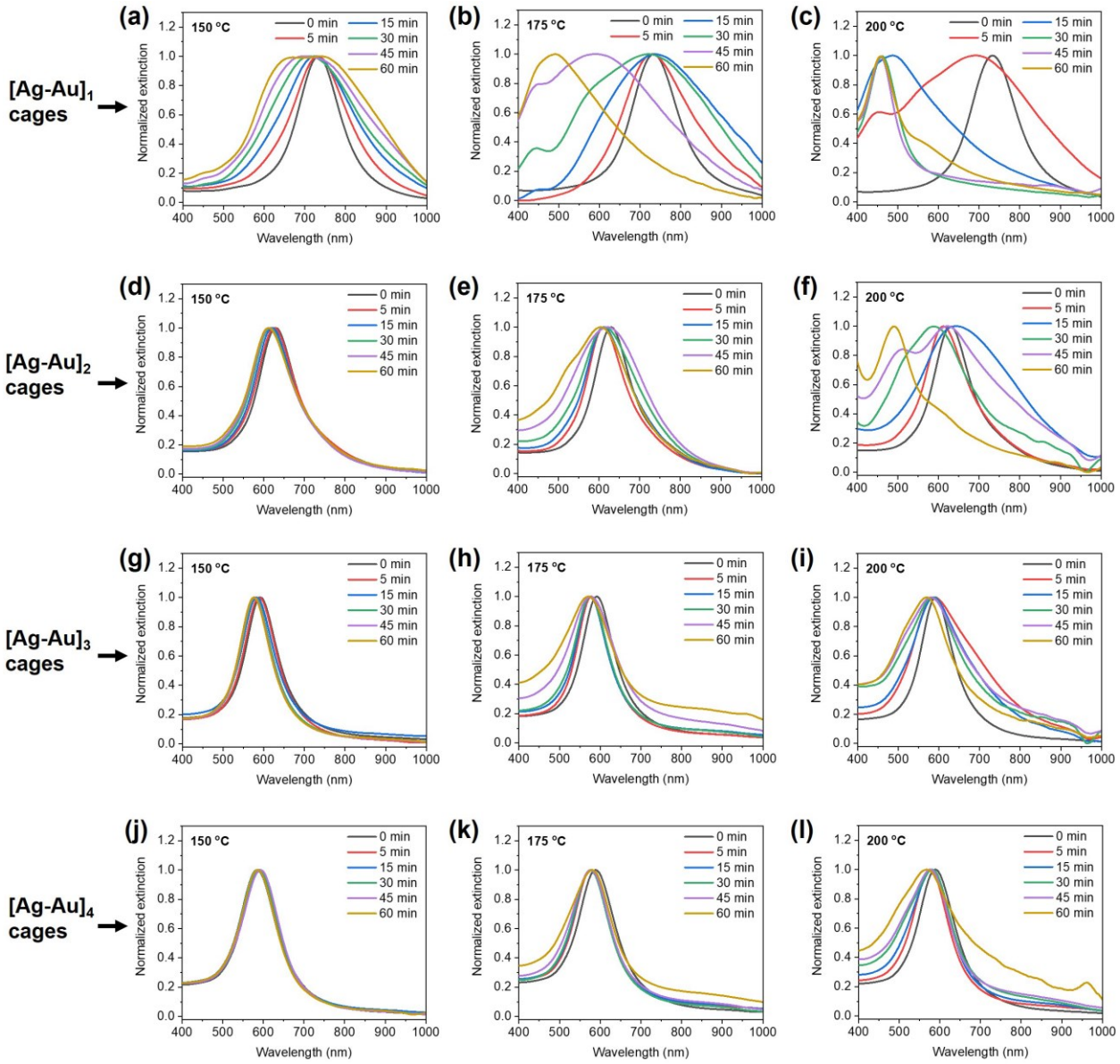

Figure 3. UV-vis spectra taken from [Ag-Au]$_n$ cages (n = 1, 2, 3, and 4) after they had been heated in diethylene glycol at different temperatures for certain periods of time. (a-c) [Ag-Au]$_1$ cages; (d-f) [Ag-Au]$_2$ cages; (g-i) [Ag-Au]$_3$ cages; (j-l) [Ag-Au]$_4$ cages.

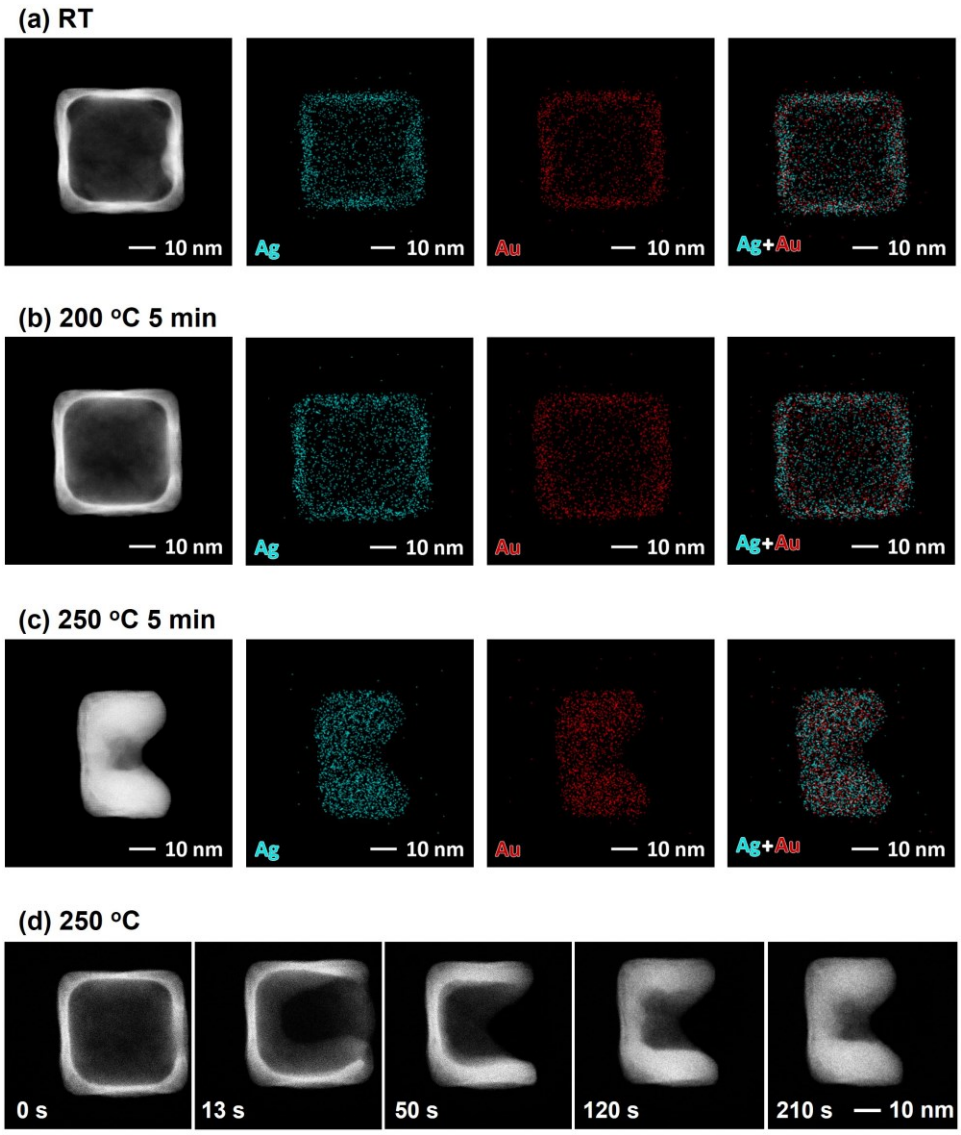

Figure 4. *In-situ* HAADF-STEM images recorded from the same $[Ag\text{-}Au]_1$ cage at: (a) room temperature (RT); (b) 200 °C after 5 min annealing; (c) 250 °C after 5 min annealing. (d) HAADF-STEM images showing the morphological changes of the $[Ag\text{-}Au]_1$ cage at 250 °C after different annealing times (0-210 seconds).

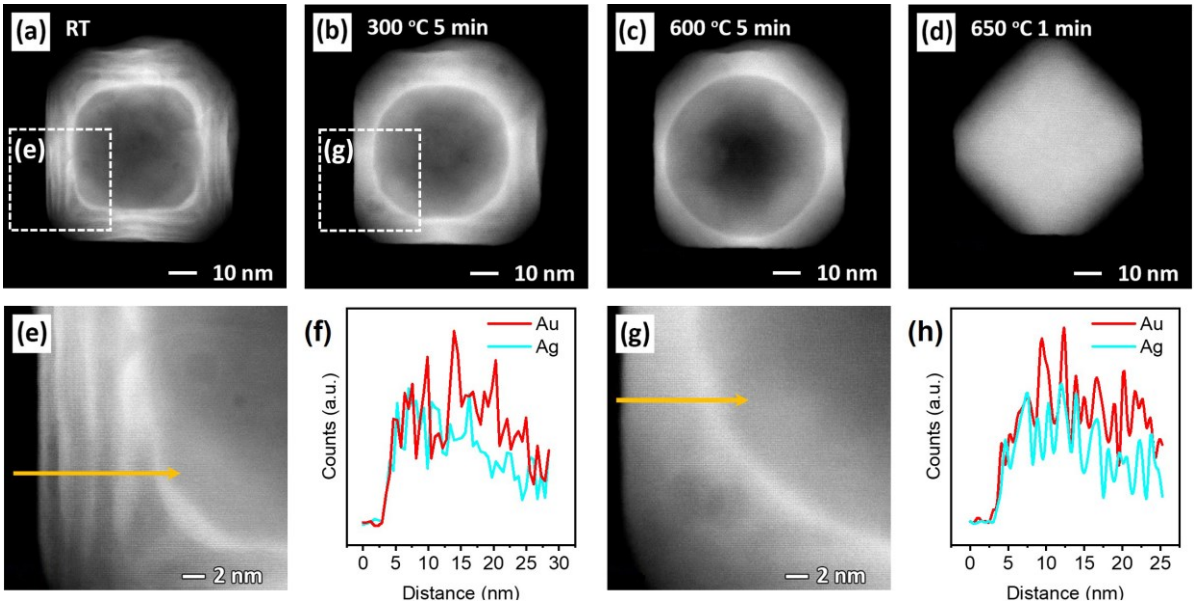

Figure 5. *In-situ* HAADF-STEM images recorded from the same $[Ag\text{-}Au]_4$ cage at: (a) room temperature (RT); (b) 300 °C after 5 min annealing; (c) 600 °C after 5 min annealing; and (d) 650 °C after 1 min annealing. (e, g) magnified HAADF-STEM images of the regions marked by dashed squares in (a) and (b), respectively. (f, h) line-scan EDS spectra of Au and Ag elements that were recorded along the arrows shown in (e) and (g), respectively.